⟳ Check for updates

Role of SiO₂ in enhancing CO yield by using silica-supported La$_{0.5}$Ba$_{0.5}$FeO$_3$ in reverse water–gas shift chemical looping†

Hanzhong Shi, Jiawei Guo, Prabhsimran Singh, Venkat R. Bhethanabotla [ID] * and John N. Kuhn [ID] *

Perovskite oxides, such as La$_{0.5}$Ba$_{0.5}$FeO$_3$ (LBF), facilitate CO₂ conversion by reverse water–gas shift chemical looping (RWSG-CL) at moderate conditions by employing an oxygen vacancy at the surface to aid CO₂ adsorption and then to scavenge an oxygen atom from it to fill the vacancy. The formation of composites with silica is also known to enhance the perovskite oxide's performance. To better clarify this, experimental and computational methods are now combined to probe CO₂ adsorption for both unsupported and silica-supported LBF. Chemisorption tests showed the CO₂ adsorption sites increased from 12.4 to 60.6 μmol g$_{LBF}$$^{-1}$ after adding SiO₂ (75 wt%) to LBF (25 wt%). Spectroscopic studies (DRIFTS) indicated that the carbonate formation during CO₂ adsorption shifts from bidentate to monodentate because the surface morphology changes upon supporting on silica. Computational (DFT) results provide evidence for CO₂ adsorbed as a monodentate and a bidentate carbonate, respectively, on the (111) and (100) surfaces. Monodentate species required lower energy, as determined by DFT, to dissociate C−O bond than bidentate species. Since XRD results identified increases in the (111) relative to (100) planes upon supporting LBF on SiO₂, the combined DRIFTS and DFT approach revealed that the perovskite oxide restructures when in composite form, which explains the increased RWGS-CL process yield of CO.


Sustainability spotlight

To deal with the massive CO₂ emissions and nearly daily news on climate change, a scalable technology to repurpose this waste to the carbon backbone of fuels and chemicals could revolutionize society. Such routes have been plagued by technical and economic challenges. Our ongoing efforts focus on converting CO₂ to CO by chemical looping using a perovskite oxide with green hydrogen as a tandem reactant. The current research investigates the mechanism of efficient conversion, with which we can design better redox materials and processes to propel this technology forward. Our project goals align with the UN sustainable development goals of clean energy (SDG 7), industry innovation (SDG 9), responsible consumption (SDG 12), and SDG 13 (climate action).

---

1 Introduction

A potential approach to repurpose CO₂ emissions is the conversion of CO₂, aided by intermittent renewable energy inputs, into valuable fuels and chemicals. An example of such an alternative pathway involves the conversion of CO₂ into CO, followed by the further conversion of CO into high-value chemical products, such as methane and other hydrocarbons with added value.[1–4] However, the pivotal step in this process, the conversion of CO₂ into CO, presents a significant challenge due to the exceptionally high energy requirement needed to break a C=O bond. This is primarily attributed to the inherent stability of the symmetric CO₂ molecule ($\Delta G = -396$ kJ mol^{-1}). To address this energy barrier and reduce the associated energy costs, researchers have explored the utilization of catalytic and non-catalytic reaction processes. A promising process is the reverse water–gas shift chemical looping (RWGS-CL).

RWGS-CL operates through a two-step reaction process. In the first reduction step (eqn (1.1)) metal oxide materials (MO$_x$) are partially reduced by reacting with hydrogen to form the oxygen vacancy. In the second oxidation step (eqn (1.2)) the oxygen vacancy on reduced; MO$_{x-\delta}$ reacts with CO₂ to produce CO. Subsequently, the regenerated oxide returns to its original structure.

$$MO_x + \delta H_2 \rightarrow MO_{x-\delta} + \delta H_2O \quad (1.1)$$

$$MO_{x-\delta} + \delta CO_2 \rightarrow MO_x + \delta CO \quad (1.2)$$
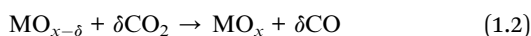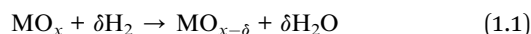
Department of Chemical, Biological, and Materials Engineering, University of South Florida, 4202 E. Fowler Ave., ENG030, Tampa, Florida 33620, USA. E-mail: bhethana@usf.edu; jnkuhn@usf.edu

† Electronic supplementary information (ESI) available. See DOI: https://doi.org/10.1039/d4su00416g

Compared to other CO_2 conversion reactions which often necessitate extremely high temperatures (generally above 1000 °C) to break the C=O bond,[1–4] RWGS-CL offers an alternative energy requirement by utilizing perovskite oxides as agent materials. In our previous research, we proposed several perovskite oxide materials to operate at a moderate temperature (~550 °C) of RWGS-CL.[5–7] Perovskite oxides (ABO_3) are composed of three essential components: an 'A' site element, a 'B' site element, and three oxygen atoms. Typically, 'A' site elements are chosen from Group II or the lanthanides, while 'B' site elements are primarily transition metals. The perovskite crystal structure exhibits stability across a wide range of compositions on each site, making it an ideal phase for tuning its properties to introduce oxygen vacancies and enhance its capacity for CO_2 adsorption.

In our previous research, $La_{0.5}Ba_{0.5}FeO_3$ (LBF) has emerged as a potential candidate for low-temperature RWGS-CL, as it is capable of converting CO_2 to CO at 480 °C with a CO yield of 0.2 mmol g^{-1} LBF.[7] To facilitate the industrial-scale use of LBF material, LBF/SiO_2 composites were synthesized by adding SiO_2 (quartz, 75 wt%) to pure LBF (25 wt%) to enhance LBF dispersion.[8,9] Subsequently, the LBF/SiO_2 powder was formed into pellets using tableting or extrusion methods. The resulting LBF/SiO_2 pellets converted CO_2 to CO at 550 °C with a CO yield of approximately 2.2 mmol g^{-1} LBF with long-term stability in 50-cycle RWGS-CL reaction.[10] Notably, the materials' CO yields were increased when compared to unsupported LBF. As summarized in Table 1, the addition of SiO_2 enriches the (111) plane of LBF crystals. This is noteworthy as previous studies have shown that the (111) surface of similarly related materials, such as MgO and NiO, exhibits higher adsorption strength compared to the (100) surface.[11,12] Therefore, the enriched (111) plane in LBF/SiO_2 composites could potentially enhance the RWGS-CL reaction, providing a plausible explanation for the observed increase in CO yield after adding SiO_2 as a support material. However, a detailed explanation requires further investigation. In this study, we aim to elucidate the surface mechanism behind this phenomenon by combining experimental and computational methods.

The computational method employed in this study is density functional theory (DFT), which has gained popularity for its ability to compute molecular structures, vibrational frequencies, and energies of chemical reactions.[13–16] DFT frequency calculations are known to be reliable and less computationally demanding.[17,18] Therefore, we have used DFT to calculate the vibrational frequencies of the species adsorbed on LBF and LBF/SiO_2 during the RWGS-CL reaction. To validate the DFT frequency results, diffuse reflectance infrared Fourier transform spectroscopy (DRIFTS) was utilized to measure the vibrational frequencies of the same samples.[19–21] These *in situ* DRIFTS experiments combined with DFT calculations were utilized to provide a comprehensive understanding of the vibrational frequencies and adsorption behavior of the species on LBF and LBF/SiO_2 materials. Mechanistic insights into factors contributing to the improved performance of the silica-supported LBF is gained from this study.

2 Materials and methods

2.1 Experimental method

2.1.1 Materials. Citric acid ($C_6H_8O_7$, CA; Aldrich, ACS reagent ≥99.5%), lanthanum(III) nitrate, ($La(NO_3)_3$, Aesar, 99.9%), barium carbonate ($BaCO_3$, Puratronic, 99.997%), iron(III) nitrate ($Fe(NO_3)_3$, Aldrich, ACS reagent ≥98%), ethylene glycol ($C_2H_6O_2$, EG; Millipore, ≥99.0%), silicon dioxide (SiO_2, Sigma-Aldrich quartz), and deionized water (H_2O > 18.0 MΩ cm^{-1}) were used as obtained.

2.1.2 Synthesis of LBF and SiO_2-supported LBF. LBF supported on SiO_2 was synthesized using a modified Pechini method.[22] The aqueous solution was made with 12 g citric acid and deionized (DI) water. The metal sources, $La(NO_3)_3$, $BaCO_3$, and $Fe(NO_3)_3$ were dissolved in the prepared solution with 2 h stirring at 90 °C until the solution turned red. Following this, ethylene glycol was added to form the gel by mixing for 6 h at 90 °C. Then, 3.6 g of SiO_2 was added into the gel and mixed for an additional 1 h at 90 °C. The gel was transferred to an alumina crucible and heated at 450 °C for 2 h at a heating rate of 20 °C min^{-1} in air. Then, after grinding the sample into fine powder it was calcined at 800 °C for 6 h in air with the same heating rate to form the LBF/SiO_2 sample. The precursor was measured to satisfy the element molar ratio of LBF (La : Ba : Fe : CA : EG = 0.5 : 0.5 : 1 : 10 : 40), and SiO_2 was added at the mass ratio of LBF/SiO_2 25 wt% (LBF : SiO_2 = 1 : 3). The LBF sample was synthesized by the same method, but without adding SiO_2 after forming the gel. Other experiments are described in ESI.†

2.1.3 DRIFTS–CO_2–adsorption experiments. For DRIFTS–CO_2–adsorption experiments, a mass of approximately 50 mg LBF or LBF/SiO_2 was placed into the reactor. The reactor was installed in the reaction chamber that was purged by dry air overnight before starting the experiments. A total gas flow rate of 50 sccm was used. The reactor was first heated to 500 °C for LBF or 550 °C for LBF/SiO_2 under Ar. Then the reduction process was conducted by flowing 10% H_2/Ar for 30 min. The reactor was cooled down to room temperature under Ar, and the background data were taken at 25 °C. The 10% CO_2/Ar was flowed for 1 h, then the reactor was purged by Ar for 30 min, the DRIFTS data were collected after gas CO_2 was removed.

Table 1 Materials conversion properties of LBF and LBF/SiO_2 (ref. 7 and 10)

	Reduction temperature (°C)	Oxidation temperature (°C)	H_2O yield (mmol g_{LBF}^{-1})	CO yield (mmol g_{LBF}^{-1})	Surface area (m^2 g^{-1})
LBF	430	480	0.2	0.2	8.9
LBF/SiO_2	580	550	2.2	2.2	3.2

Although both DFT and DRIFTS analyses in this study were conducted at temperatures lower than those used in the actual RWGS-CL reaction. The surface properties of the materials remain relatively stable as the temperature increases from room temperature to reaction temperature, given that both the perovskite and SiO_2 are stable materials which are synthesized at a temperature much higher than reaction temperature. Therefore, it is reasonable to assume that the nature of the surface sites and the form of CO_2 adsorption remain consistent across the different temperatures.[23,24]

2.2 Computational methods

The DFT calculations in this study were performed using Quantum ESPRESSO software (Version 6.2.1).[25,26] The materials models used in the calculations are referenced from the materials project database, with corresponding index numbers.[27] The plane wave basis set and gradient generalization approximation for electron densities were used.[28,29] The projector augmented wave (PAW) potentials and Perdew–Burke–Ernzerhof (PBE) variant of exchange-correlation functional were employed.[30,31] In this study, the energy convergence criterion was set to 10^{-6} eV per atom, and the force convergence criterion was set to 0.005 eV $Å^{-1}$. A constant cutoff of 40 Ry (544 eV) was selected. A k-point mesh of $(4 \times 4 \times 1)$ was used for the Brillouin zone sampling. The Hubbard U correction was not applied in this calculation, as the trend of energies did not show a significant shift with or without the application of the Hubbard U correction.[32,33] The vibrational frequency was calculated from a 6×6 Hessian matrix.[34] The details of DFT calculation and other experimental methods are described in ESI.†

3 Result and discussion

3.1 Materials characterizations

To better understand the reason for LBF/SiO_2 giving larger CO yield than LBF in the RWGS-CL process, XRF, XRD, and XPS experiments were performed on both materials. The metal elemental compositions of the samples were determined by XRF
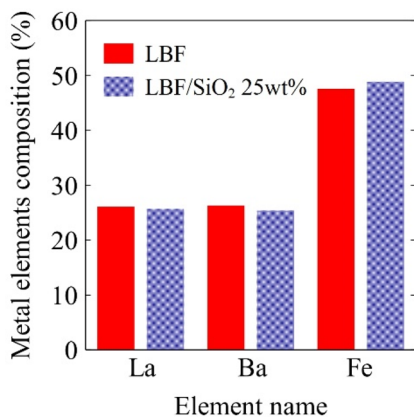

Fig. 1 Metal elemental compositions of fresh samples in bulk calculated from XRF results, red solid bar is LBF result, and blue dotted bar is for LBF/SiO_2 25 wt%.

(Fig. 1), showing that LBF has 26.1% La, 26.3% Ba, and 47.6% Fe, while LBF/SiO_2 (25 wt%) has 25.7% La, 25.4% Ba, and 48.9% Fe, which are close to the nominal compositions.

The XRD results (Fig. 2) indicate that LBF/SiO_2 structure is enriched with the (111) planes, as evidenced by the intensity ratio of diffraction lines ((111) to (110)) switching from 0.2 to 1, because the relative intensities generally correlate with a greater number of crystallites oriented along a specific plane.[35] This switch of crystallographic planes could be because SiO_2 influences the preferential growth or orientation of the active catalytic phase.[36] As demonstrated in our previous study, SiO_2 exhibits a wettability effect on the perovskite particles, potentially leading to the formation of a secondary plane associated with surface wetting.[37] Thus, the presence of SiO_2 and the synthesis method can stabilize (111) planes more than others (110), leading to an increased intensity in the XRD pattern.[38] LBF is used as the control sample for the (100) plane. The surface morphology difference is also observed from XPS results (Fig. 3). After adding SiO_2 to LBF, there is a noticeable shift in the difference of La3d$_{5/2}$ binding energy from 4.1 to 4.0 eV, and a shift in the difference of La3d$_{3/2}$ binding energy from 3.4 to 3.1 eV. The binding energy differences between two La3d peaks are close between LBF and LBF/SiO_2. The binding energy of O1s exhibits a distinct difference due to the presence of oxygen bonds from SiO_2. Fe and Ba remain the same. Therefore, by combing the results from XRF, XRD, and XPS, the surface with enriched (111) is a potential reason that led to increase in the CO yield.

3.2 CO_2 chemisorption

To better understand the CO_2 adsorption on LBF and LBF/SiO_2, CO_2 chemisorption experiments were performed on these two reduced samples at room temperature (Fig. 4). Results indicate a similar volume of CO_2 adsorbed by LBF and LBF/SiO_2. However, a sample of SiO_2 support material was tested to find that SiO_2 is inert for CO_2 chemisorption, and the concentration of perovskite in LBF (100%) is 4 times than LBF/SiO_2 (25 wt%). Therefore, an increased CO_2 chemisorption upon supporting in SiO_2, increasing from 12.4 μmol g_{LBF}^{-1} (LBF) to 60.6 μmol g_{LBF}^{-1} (LBF/SiO_2) calculated by extrapolation method (eqn (S3)†).[39,40] From these results, we conclude that supporting LBF on SiO_2 enhances of the number of CO_2 chemisorption sites, by a factor of 5 in this case. This enhancement can be considered as one reason the improved CO yield in the reduction process.

3.3 Temperature-programmed oxidation experiments

Oxygen vacancies are created during the reduction phase of the RWGS-CL process. The perovskite phase, $La_{0.5}Ba_{0.5}FeO_3$, is reduced to $La_{0.5}Ba_{0.5}FeO_{3-\delta}$, where δ presents oxygen vacancy amount that is 0.1 and 0.5 for LBF and LBF/SiO_2. respectively.[7,10] The oxidation temperatures for samples of reduced LBF and reduced LBF/SiO_2 were examined under various oxidizers (O_2, H_2O, and CO_2) using TPO experiments. Comparing the results from TPO-O_2, TPO-H_2O, and TPO-CO_2 experiments (Fig. 5), it is evident that a lower oxidation temperature of 250 °C is required for O_2, which is the strongest oxidizer, compared to H_2O and
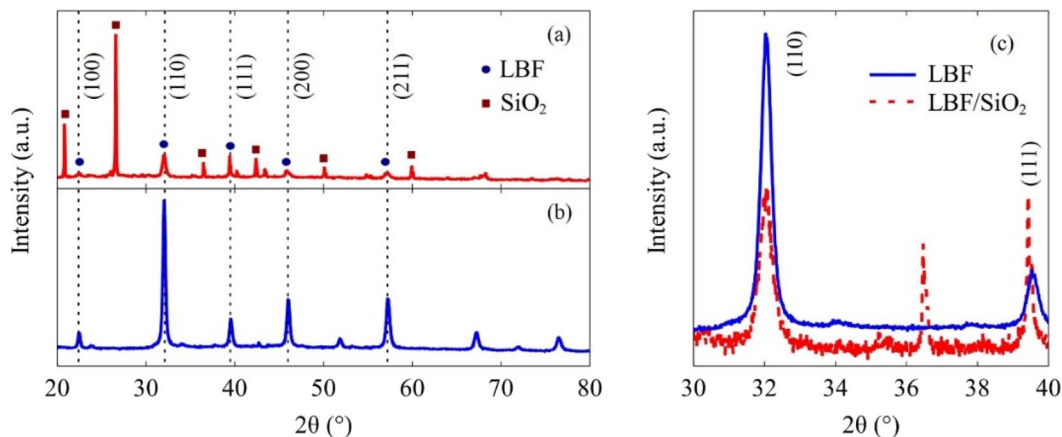
Fig. 2 XRD results of synthesized samples. (a) LBF/SiO$_2$, circular marker denotes the crystal planes from LBF, and rectangular marker denotes the crystal planes from SiO$_2$. (b) LBF. (c) Detailed results in the 2θ range of 30 to 40°.

CO$_2$, both of which require temperatures exceeding 400 °C. For the reduced LBF/SiO$_2$, a second oxidation peak appears at 530 °C, indicating a shift in surface morphology due to the addition of SiO$_2$. Interestingly, the oxidation temperatures for H$_2$O and CO$_2$ are similar, deviating from the expectation that H$_2$O, typically a stronger oxidizer than CO$_2$, would oxidize the sample at a lower temperature. This anomaly is attributed to the oxygen vacancies on the perovskite oxide surface, which enhance CO$_2$ adsorption and lower the dissociation energy of CO$_2$ making CO$_2$ a strong oxidant in this reaction Consequently, this reduced energy requirement aligns with the lower temperature range (400 to 650 °C) for the CO$_2$ to CO reaction in the RWGS-CL process, compared to the higher temperatures (>1000 °C) required in conventional thermochemical processes.

3.4 DRIFTS–CO$_2$–adsorption

DRIFTS–CO$_2$–adsorption experiments were conducted to reduce the LBF and LBF/SiO$_2$ (25 wt%) samples. The DRIFTS results (Fig. 6) show the vibrational frequencies of the adsorbed
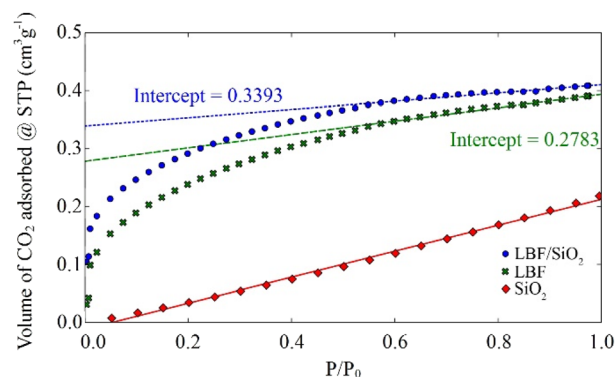

Fig. 4 Isotherms for CO$_2$ adsorption at room temperature.

species. The experimental vibrational frequencies are $\nu_{as} = 1606$ cm^{-1} and $\nu_s = 1347$ cm^{-1} for CO$_2$ adsorbed on reduced LBF, and $\nu_{as} = 1544$ cm^{-1} and $\nu_s = 1364$ cm^{-1} for CO$_2$ adsorbed on reduced LBF/SiO$_2$ (25 wt%). The difference between ν_{as} and ν_s decreases from 259 to 180 cm^{-1}. This is because CO$_2$ is
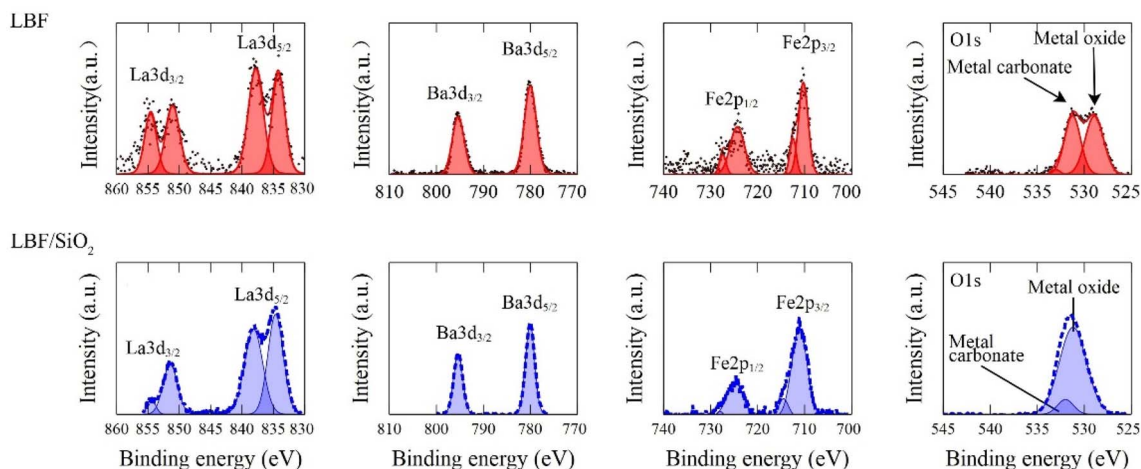

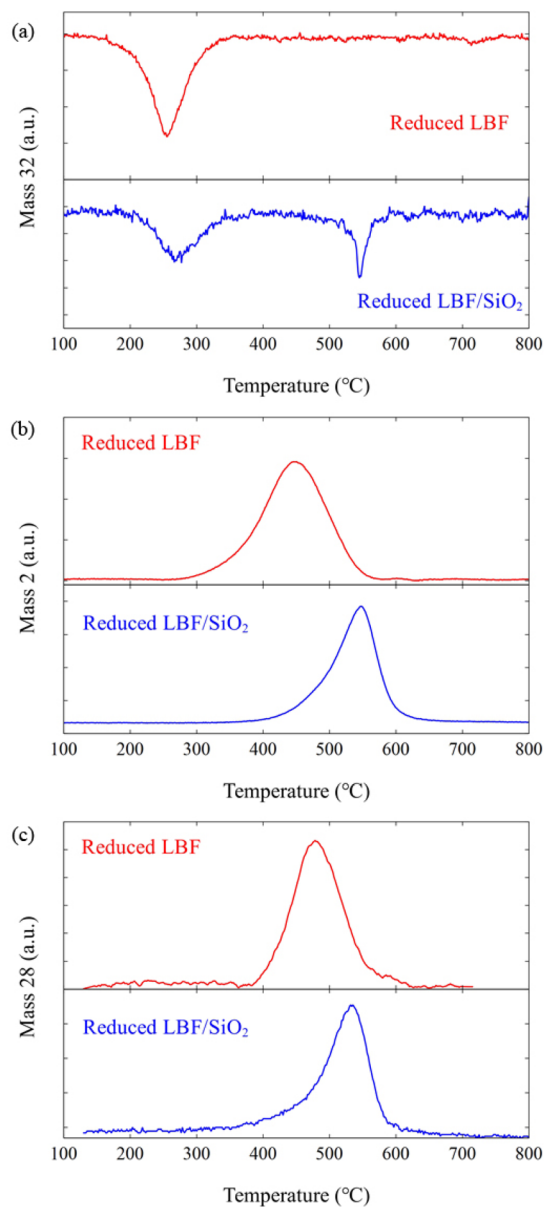**Fig. 3** XPS results for LBF (red, top) and LBF/SiO$_2$ (blue, bottom).

Fig. 5 TPO results for different oxidizers: (a) TPO-O_2, (b) TPO-H_2O, and (c) TPO-CO_2. The red lines (top) are the results for reduced LBF, and the blue lines (bottom) are the results for reduced LBF/SiO_2.
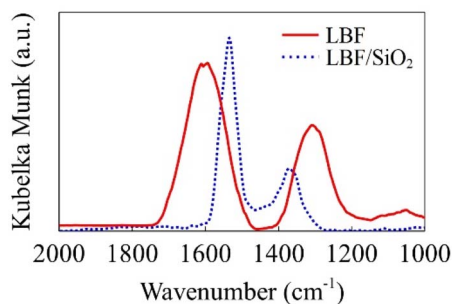

Fig. 6 DRIFT spectra of TPD-CO_2 experiments. Red solid line is the result for LBF, and blue dotted line is the result for LBF/SiO_2 25 wt%.

adsorbed in the bidentate carbonate form on LBF whereas it is adsorbed in the monodentate carbonate form on LBF/SiO_2.[41] This carbonate formation differences agree with the DFT calculations presented in the next section.

3.5 DFT calculations

3.5.1 Oxygen vacancy formation energy (E_{Ovac}). The surface constructions for LBF-111 and LBF-100, along with the possible sites of oxygen vacancy, are shown in Fig. S1.† The oxygen vacancy formation energy (Table 2) was calculated using the method described in ESI.† E_{Ovac} of LBF-100 with Fe surface (LBF-100(Fe)) was found to be slightly lower than that of La/Ba surface (LBF-100(La/Ba)), indicating that the Fe surface is more favorable for oxygen vacancy formation during the reduction process. Similarly, for the LBF-111 structure, Fe–O is the most likely site for reduction. Comparing the E_{Ovac} values of LBF-111 and LBF-100, it was found that E_{Ovac} of LBF-111 (1.62 and 1.80 eV) is significantly lower than E_{Ovac} of LBF-100 (3.01 and 3.24 eV), indicating that LBF-111 is the preferred surface for providing oxygen vacancies in the reduction step of RWGS-CL.

3.5.2 CO_2 adsorption structure. In the oxidation step of RWGS-CL, CO_2 molecules adsorb on the oxygen-vacated LBF surface. The physisorbed and chemisorbed CO_2 are identified based on a distance of 1.43 Å.[42,43] Possible chemisorbed structures of CO_2 on LBF-111 are shown in Fig. 7(a)–(g), while one structure for LBF-100 (Fe–O) is shown in Fig. 7(i), based on the possible sites of oxygen vacancy as shown in Fig. S1.† The surface structure of (111) is named by surface atoms, for example, LBF-111(LaBa–La) means two La and one Ba atoms with one La atom on the center of the LBF (111) surface. The C=O bond distances between carbon and oxygen are presented in Table 3. C=O bond lengths falling within the range of 1.21 to 1.23 Å indicate the formation of a double bond between carbon and oxygen, while bond lengths of C–O_a and C–O_b (Table 3) in the range of 1.26 to 1.34 Å are considered as C–O single bonds.[44] Therefore, the DFT calculations suggest that CO_2 adsorption occurs in the carbonate form. In (Fig. 7(g) & (h)), the bond lengths of 1.16 and 1.17 Å for LBF-111(BaLa–Ba) do not follow the same trend, which could be attributed to Ba not being a site for CO_2 adsorption.

3.5.3 Vibrational frequency of adsorbed CO_2. The CO_2 adsorption structure on the (111) plane was selected as LBF-111(BaLa–Fe) (Fig. 7(f)), while the adsorption structure on the (100) plane is shown in Fig. 7(i). The vibrational frequencies obtained from DFT calculations and DRIFTS results are shown in Table 4. The vibrational frequencies of CO_2 on LBF-100(Fe–O) are $\nu_{as} = 1663$ cm^{-1} and $\nu_s = 1415$ cm^{-1}, while the vibrational frequencies of CO_2 on LBF-111(BaLa–Fe) are $\nu_{as} = 1639$ cm^{-1} and $\nu_s = 1450$ cm^{-1}.

Table 2 Oxygen vacancy formation energy results

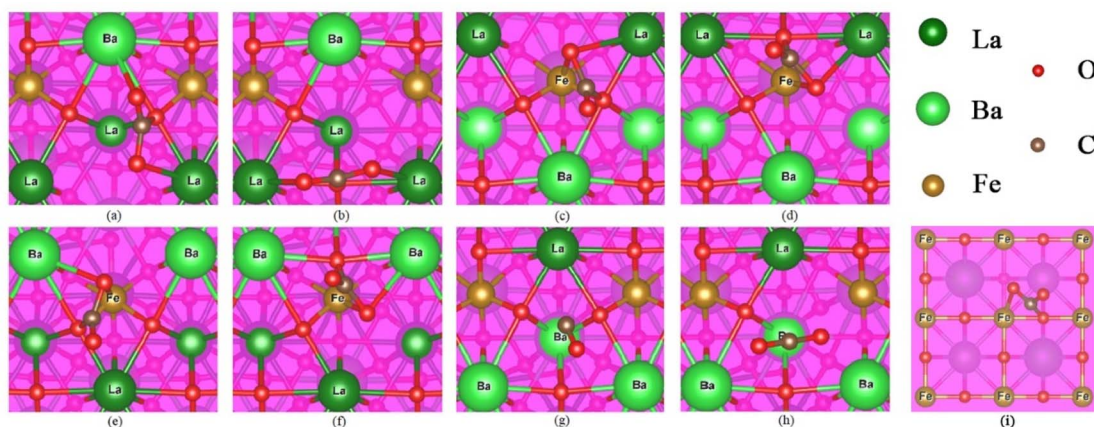| E_{Ovac} (eV)	Fe surface	La/Ba surface
LBF-111	1.62	1.80
LBF-100	3.01	3.24

Fig. 7 The CO_2 adsorption on each configuration. (a) & (b) are the adsorption results of LBF-111(LaBa–La). (c) & (d) are the adsorption results of LBF-111(LaBa–Fe), (e) & (f) are the adsorption results of LBF-111(BaLa–Fe). (g) & (h) are the adsorption results of LBF-111(BaLa–Ba), $C–O_b$ in (g) is not marked because it is away to the ideal range. (i) Is the adsorption result of LBF-100(Fe–O).

Table 3 The C–O bond lengths of the adsorbed CO_2 on LBF-111 and LBF-100 surface

	C=O bond length (Å)	$C–O_a$ bond length (Å)	$C–O_b$ bond length (Å)
LBF-111(LaBa–La)$_1$	1.23	1.48	1.28
LBF-111(LaBa–La)$_2$	1.23	1.44	1.26
LBF-111(LaBa–Fe)$_1$	1.21	1.43	1.32
LBF-111(LaBa–Fe)$_2$	1.21	1.41	1.34
LBF-111(BaLa–Fe)$_1$	1.22	1.42	1.32
LBF-111(BaLa–Fe)$_2$	1.22	1.41	1.33
LBF-111(BaLa–Ba)$_1$	1.16	1.16	—
LBF-111(BaLa–Ba)$_2$	1.17	1.17	—
LBF-100(Fe–O)	1.22	1.40	1.37

Table 4 Vibrational frequency (cm^{-1}) results from DFT calculations and DRIFTS experiments

Vibration type (surface)	DFT	DRIFTS
ν_{as} (100)	1663	1606
ν_s (100)	1415	1347
ν_δ(100)	248	259
ν_{as} (111)	1639	1544
ν_s (111)	1450	1364
ν_δ (111)	189	180

In comparison, the frequency differences (ν_δ) between antisymmetric (ν_{as}) and symmetric (ν_s) vibrations from DFT calculation results are 248 cm^{-1} and 189 cm^{-1}. Although there are slight differences between the calculated vibrational frequencies and the experimental data due to the limitations of DFT calculations,[45,46] the ν_δ values are in agreement. In this study, the calculated ν_δ of CO_2 on reduced LBF is 189 cm^{-1}, which is close to the experimental value of 180 cm^{-1}, while the calculated ν_δ of CO_2 on reduced LBF/SiO_2 (25 wt%) is 248 cm^{-1}, which is close to the experimental value of 259 cm^{-1}. Thus, it can be concluded that CO_2 is adsorbed in the form of

carbonates during the oxidation step in RWGS-CL. The vibrational frequency difference between antisymmetric and symmetric vibrations decreases after adding SiO_2 as a support material, indicating that the adsorbed CO_2 on the (111) plane is monodentate carbonate different from bidentate carbonate on the (100) plane due to the difference of ν_δ in carbonate species.[41,47,48]

3.5.4 Reaction intermediate energy and mechanism of oxidation step in RWGS-CL. The energy diagram in Fig. 8 illustrates the energy changes for each intermediate state during the RWGS-CL process by LBF-111 (BaLa–Fe) and LBF-100 (Fe–O). The initial state (IS, $E_{IS} = 0$) is the fresh LBF surface, which is also the final state (FS) after the reaction. The adsorption structures are shown in Fig. S2.† The total energy difference (E_{IMx}) between each intermediate state (IMx) and IS are as follows:

(1) IS – IM1: H_2 is physisorbed on the original surface, resulting in an energy change of $E_{IM1(100)} = -0.014$ eV for the (100) plane and $E_{IM1(111)} = -0.006$ eV for the (111) plane.

(2) IM1 – IM2: the physisorbed H_2 moves closer to the surface and forms a chemisorption state, resulting in an energy change
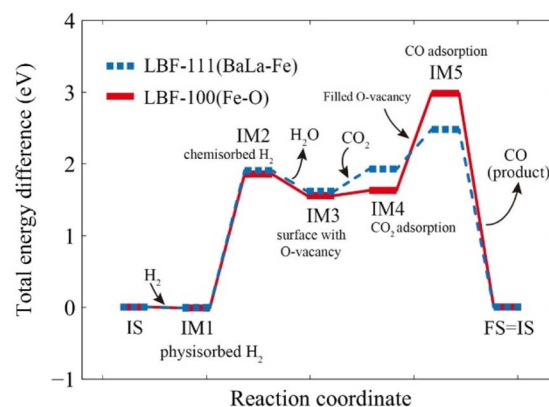

Fig. 8 Step reaction energy for RWGS-CL. Red solid line is the reaction on (100) plane, and blue dotted line is the reaction on (111) plane.

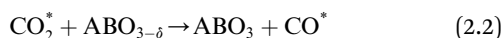of $E_{IM2(100)} = 1.85$ eV for the (100) plane and $E_{IM2(111)} = 1.91$ eV for the (111) plane.

(3) IM2 – IM3: the samples are reduced with adsorbed H_2, resulting in the formation of oxygen vacancies on the surface and production of H_2O, with an energy change of $E_{IM3(100)} = 1.55$ eV for the (100) plane and $E_{IM3(111)} = 1.62$ eV for the (111) plane.

(4) IM3 – IM4: CO_2 is adsorbed on the reduced surface as carbonate form, resulting in an energy change of $E_{IM4(100)} = 1.63$ eV for the (100) plane and $E_{IM4(111)} = 1.93$ eV for the (111) plane.

(5) IM4 – IM5: adsorbed CO_2 is converted to CO by oxidizing the oxygen-vacated surface, and the produced CO is adsorbed on the surface, resulting in an energy change of $E_{IM5(100)} = 2.98$ eV for the (100) plane and $E_{IM5(111)} = 2.48$ eV for the (111) plane.

(6) IM5 – FS: CO is desorbed, and the surface regains its original structure.

The intermediate energy results indicate that the reaction on the (111) plane requires a lower maximum energy (2.48 eV) compared to the reactions on the (100) plane (2.98 eV), which suggests that the (111) plane has the potential to produce a higher amount of CO at the same temperature. The reduction steps occur from IS to IM3, while the oxidation steps are described in eqn (2.1) to (2.3).

$$\delta CO_2 + * \rightarrow \delta CO_2^* \qquad (2.1)$$

$$CO_2^* + ABO_{3-\delta} \rightarrow ABO_3 + CO^* \qquad (2.2)$$

$$CO^* \rightarrow CO + * \qquad (2.3)$$

4 Conclusion

Previous studies reported the increases of CO yield upon supporting on SiO_2. To better describe the fundamental reason, this research focused particularly on the CO_2 adsorption on both LBF and LBF/SiO_2 surfaces during the oxidation step in RWGS-CL. X-ray diffraction (XRD) analysis revealed a morphology alteration upon SiO_2 addition, notably a relative increase in the exposed (111) planes. TPD-CO_2 combined with DRIFTS experiments further demonstrate CO_2 adsorption as carbonate on the reduced perovskite surfaces. CO_2 chemisorption shows CO_2 sites increased from 12.4 to 60.6 μmol g_{LBF}^{-1} after adding SiO_2.

TPO experiments under various oxidizers highlight the role of oxygen vacancies on the reduced perovskite surface. DFT calculations provided insight into the adsorption energy and structure of carbonate on different planes, identifying monodentate carbonate on the (111) plane and bidentate carbonate on the (100) plane, distinguished by variations in the carbonate species' stretching modes.

In situ DRIFTS further confirmed these findings, correlating specific ν_δ to monodentate and bidentate carbonate structures on the (111) and (100) planes, respectively. DFT calculations of the energy profiles for reaction intermediates suggest that the

(111) surface offers a lower energy pathway for converting CO_2 to CO. Collectively, these results elucidate the role of SiO_2 in enhancing CO yield as the increased (111) planes facilitate monodentate carbonate formation, thereby reducing the energy requirement for converting CO_2 to CO.

Data availability

The data supporting this article have been included as part of the ESI.†

Conflicts of interest

J. N. K. and V. R. B. declare patents and other financial interests in this technology.

Acknowledgements

References

1 Q. Jiang, J. Tong, G. Zhou, Z. Jiang, Z. Li and C. Li, *Sol. Energy*, 2014, **103**, 425–437.

2 A. Le Gal and S. Abanades, *J. Phys. Chem. C*, 2012, **116**, 13516–13523.

3 F. Fresno, R. Fernández-Saavedra, M. Belén Gómez-Mancebo, A. Vidal, M. Sánchez, M. Isabel Rucandio, A. J. Quejido and M. Romero, *Int. J. Hydrogen Energy*, 2009, **34**, 2918–2924.

4 C. Agrafiotis, M. Roeb and C. Sattler, *Renewable Sustainable Energy Rev.*, 2015, **42**, 254–285.

5 Y. A. Daza, D. Maiti, B. J. Hare, V. R. Bhethanabotla and J. N. Kuhn, *Surf. Sci.*, 2016, **648**, 92–99.

6 A. E. Ramos, D. Maiti, Y. A. Daza, J. N. Kuhn and V. R. Bhethanabotla, *Catal. Today*, 2019, **338**, 52–59.

7 H. Shi, V. R. Bhethanabotla and J. N. Kuhn, *J. CO2 Util.*, 2021, **51**, 101638.

8 B. J. Hare, D. Maiti, Y. A. Daza, V. R. Bhethanabotla and J. N. Kuhn, *ACS Catal.*, 2018, **8**, 3021–3029.

9 J. C. Brower, B. J. Hare, V. R. Bhethanabotla and J. N. Kuhn, *ChemCatChem*, 2020, **12**, 6317–6328.

10 H. Shi, V. R. Bhethanabotla and J. N. Kuhn, *J. Ind. Eng. Chem.*, 2023, **118**, 44–52.

11 H. Onishi, C. Egawa, T. Aruga and Y. Iwasawa, *Surf. Sci.*, 1987, **191**, 479–491.

12 J. Hu, K. Zhu, L. Chen, C. Kübel and R. Richards, *J. Phys. Chem. C*, 2007, **111**, 12038–12044.

13 J. K. Labanowski and J. W. Andzelm, *Density Functional Methods in Chemistry*, Springer Science & Business Media, 2012.

14 P. Politzer and J. M. Seminario, *Modern Density Functional Theory: a Tool for Chemistry*, Elsevier, 1995.

15 R. G. Parr and Y. Weitao, *Density-Functional Theory of Atoms and Molecules*, Oxford University Press, 1995.

16 T. Ziegler, *Chem. Rev.*, 1991, **91**, 651–667.

17 M. W. Wong, *Chem. Phys. Lett.*, 1996, **256**, 391–399.

18 L. J. Bartolotti and K. Flurchick, *Rev. Comput. Chem.*, 1996, **7**, 187–216.

19 N. H. Elsayed, D. Maiti, B. Joseph and J. N. Kuhn, *Catal. Lett.*, 2018, **148**, 1003–1013.

20 G. H. Smudde, T. L. Slager, C. G. Coe, J. E. MacDougall and S. J. Weigel, *Appl. Spectrosc.*, 1995, **49**, 1747–1755.

21 H. Gao, H. He, Y. Yu and Q. Feng, *J. Phys. Chem. B*, 2005, **109**, 13291–13295.

22 M. Popa and M. Kakihana, *Solid State Ionics*, 2002, **151**, 251–257.

23 M. Bersani, K. Gupta, A. K. Mishra, R. Lanza, S. F. R. Taylor, H.-U. Islam, N. Hollingsworth, C. Hardacre, N. H. de Leeuw and J. A. Darr, *ACS Catal.*, 2016, **6**, 5823–5833.

24 L. F. Rasteiro, R. A. De Sousa, L. H. Vieira, V. K. Ocampo-Restrepo, L. G. Verga, J. M. Assaf, J. L. F. Da Silva and E. M. Assaf, *Appl. Catal., B*, 2022, **302**, 120842.

25 P. Giannozzi, O. Andreussi, T. Brumme, O. Bunau, M. Buongiorno Nardelli, M. Calandra, R. Car, C. Cavazzoni, D. Ceresoli, M. Cococcioni, N. Colonna, I. Carnimeo, A. Dal Corso, S. de Gironcoli, P. Delugas, R. A. DiStasio, A. Ferretti, A. Floris, G. Fratesi, G. Fugallo, R. Gebauer, U. Gerstmann, F. Giustino, T. Gorni, J. Jia, M. Kawamura, H. Y. Ko, A. Kokalj, E. Küçükbenli, M. Lazzeri, M. Marsili, N. Marzari, F. Mauri, N. L. Nguyen, H. V. Nguyen, A. Otero-de-la-Roza, L. Paulatto, S. Poncé, D. Rocca, R. Sabatini, B. Santra, M. Schlipf, A. P. Seitsonen, A. Smogunov, I. Timrov, T. Thonhauser, P. Umari, N. Vast, X. Wu and S. Baroni, *J. Phys.: Condens. Matter*, 2017, **29**, 465901.

26 K. Burke, *J. Chem. Phys.*, 2012, **136**, 150901.

27 A. Jain, S. P. Ong, G. Hautier, W. Chen, W. D. Richards, S. Dacek, S. Cholia, D. Gunter, D. Skinner, G. Ceder and K. A. Persson, *APL Mater.*, 2013, **1**, 011002.

28 P. Giannozzi, S. Baroni, N. Bonini, M. Calandra, R. Car, C. Cavazzoni, D. Ceresoli, G. L. Chiarotti, M. Cococcioni, I. Dabo, A. Dal Corso, S. de Gironcoli, S. Fabris, G. Fratesi, R. Gebauer, U. Gerstmann, C. Gougoussis, A. Kokalj, M. Lazzeri, L. Martin-Samos, N. Marzari, F. Mauri, R. Mazzarello, S. Paolini, A. Pasquarello, L. Paulatto, C. Sbraccia, S. Scandolo, G. Sclauzero, A. P. Seitsonen, A. Smogunov, P. Umari and R. M. Wentzcovitch, *J. Phys.: Condens. Matter*, 2009, **21**, 395502.

29 K. F. Garrity, J. W. Bennett, K. M. Rabe and D. Vanderbilt, *Comput. Mater. Sci.*, 2014, **81**, 446–452.

30 G. Kresse and D. Joubert, *Phys. Rev. B*, 1999, **59**, 1758–1775.

31 J. P. Perdew, K. Burke and M. Ernzerhof, *Phys. Rev. Lett.*, 1996, **77**, 3865–3868.

32 D. Maiti, Y. A. Daza, M. M. Yung, J. N. Kuhn and V. R. Bhethanabotla, *J. Mater. Chem. A*, 2016, **4**, 5137–5148.

33 I. W. Boateng, R. Tia, E. Adei, N. Y. Dzade, C. R. A. Catlow and N. H. de Leeuw, *PCCP Phys. Chem. Chem. Phys.*, 2017, **19**, 7399–7409.

34 D. S. Sholl and J. A. Steckel, *Density Functional Theory: a Practical Introduction*, John Wiley & Sons, 2011.

35 L. Zhang, A. A. S. Gonçalves and M. Jaroniec, *RSC Adv.*, 2020, **10**, 5585–5589.

36 R. A. McKee, F. Walker and M. Chisholm, *Phys. Rev. Lett.*, 1998, **81**, 3014.

37 D. M. Bryan, J. Hare, Y. A. Daza, V. R. Bhethanabotla and J. N. Kuhn, *ACS Catal.*, 2018, **8**, 3021–3029.

38 J. Arenas-Alatorre, M. Avalos-Borja and G. Díaz, *Appl. Surf. Sci.*, 2002, **189**, 7–17.

39 S. Brunauer, P. H. Emmett and E. Teller, *J. Am. Chem. Soc.*, 1938, **60**, 309–319.

40 C. Chen and W.-S. Ahn, *Chem. Eng. J.*, 2011, **166**, 646–651.

41 K. Coenen, F. Gallucci, B. Mezari, E. Hensen and M. van Sint Annaland, *J. CO2 Util.*, 2018, **24**, 228–239.

42 G. Pacchioni, *Surf. Sci.*, 1993, **281**, 207–219.

43 F. H. Allen and A. J. Kirby, *J. Am. Chem. Soc.*, 1984, **106**, 6197–6200.

44 J. Demaison and A. G. Császár, *J. Mol. Struct.*, 2012, **1023**, 7–14.

45 A. A. El-Azhary and H. U. Suter, *J. Phys. Chem.*, 1996, **100**, 15056–15063.

46 M. L. Laury, M. J. Carlson and A. K. Wilson, *J. Comput. Chem.*, 2012, **33**, 2380–2387.

47 B. H. Solis, Y. Cui, X. Weng, J. Seifert, S. Schauermann, J. Sauer, S. Shaikhutdinov and H.-J. Freund, *Phys. Chem. Chem. Phys.*, 2017, **19**, 4231–4242.

48 J. Liu, Y. Li, H. Liu and D. He, *Biomass Bioenergy*, 2018, **118**, 74–83.